Simultaneous Structural and Electronic Transitions in Epitaxial $VO_2/TiO_2(001)$

Galo J. Paez,[1] Christopher N. Singh,[1] Matthew J. Wahila,[2] Keith E. Tirpak,[1] Nicholas F. Quackenbush,[1] Shawn Sallis,[2] Hanjong Paik,[3,4] Yufeng Liang,[5] Darrell G. Schlom,[3,6] Tien-Lin Lee,[7] Christoph Schlueter,[7] Wei-Cheng Lee,[1] and Louis F. J. Piper[1,2,*]

[1]*Department of Physics, Binghamton University, State University of New York, Binghamton, New York 13850, USA*
[2]*Materials Science and Engineering, Binghamton University, State University of New York, Binghamton, New York 13850, USA*
[3]*Department of Materials Science and Engineering, Cornell University, Ithaca, New York 14853-1501, USA*
[4]*Platform for the Accelerated Realization, Analysis, and Discovery of Interface Materials (PARADIM), Cornell University, Ithaca, New York 14853, USA*
[5]*The Molecular Foundry, Lawrence Berkeley National Laboratory, Berkeley, California 94720, USA*
[6]*Kavli Institute at Cornell for Nanoscale Science, Ithaca, New York 14853, USA*
[7]*Diamond Light Source Ltd., Harwell Science and Innovation Campus, Didcot OX11 0DE, United Kingdom*

(Received 20 November 2019; revised manuscript received 21 February 2020; accepted 21 April 2020; published 13 May 2020)

Recent reports have identified new metaphases of VO_2 with strain and/or doping, suggesting the structural phase transition and the metal-to-insulator transition might be decoupled. Using epitaxially strained VO_2/TiO_2 (001) thin films, which display a bulklike abrupt metal-to-insulator transition and rutile to monoclinic transition structural phase transition, we employ x-ray standing waves combined with hard x-ray photoelectron spectroscopy to simultaneously measure the structural and electronic transitions. This x-ray standing waves study elegantly demonstrates the structural and electronic transitions occur concurrently within experimental limits (± 1 K).

DOI: 10.1103/PhysRevLett.124.196402

Introduction.—Mott memristor devices, where the resistance switching is driven by electron correlation effects, are considered important for emerging technologies, including resistive memory and neuromorphic computing [1,2], smart energy and solar energy storage [3–5], and terahertz device applications [6,7]. The typical activation timescale of Mott memristors is on the order of nanoseconds [8,9] and the writing or reading peak electric potential energy is tens of femtojoules [10] scalable with the device size.

The fast activation of Mott memristors is typically attributed to the existence of a pure Mott transition in which the competition between on-site Coulomb energy (U) and the delocalization energy (W) [11] causes a sudden resistance switching or metal-insulator transition, without the need for a structural transition [12]. Nevertheless, even in archetypal Mott systems, including V_2O_3 and VO_2, Mott physics (electron correlation) always interacts with other degrees of freedom during the metal-to-insulator transition (MIT) [13,14]. For example, V_2O_3 is known to undergo a MIT accompanied by a structural phase transition (SPT) between corundum and monoclinic phases [14], while VO_2 undergoes a SPT from monoclinic to rutile [15]. Of these systems, VO_2 is the most contentious because of a long-standing debate regarding the degree of Mott physics driving the transition [16,17], whereas V_2O_3 is commonly accepted as an archetypical Mott system even though its MIT and SPT are coupled [14]. It remains unclear whether the structural and electronic transitions of these systems can ever be fully decoupled.

Bulk VO_2 displays a triple phase point, where the low-temperature, insulating, monoclinic phase ($M1$) and the high-temperature, rutile, metallic phase (R) coexists with an intermediate, insulating phase ($M2$) wherein half of the V-V chains dimerize [18]. The underlying MIT in this system is described as a cooperative Mott-Peierls transition [19,20]. The delicate interplay between lattice, orbital, and spin degrees of freedom gives rise to rich physics where additional correlated phases might exist decoupled from the underlying structural transition. For example, while the system typically transitions between the $M1$ and R phases, the intermediate $M2$ phase can be stabilized in some biaxially strained VO_2 films [18,21], as strain has been shown to significantly modify the degree of electron correlations expressed by the (U/W) [22,23]. Some reports have even suggested the existence of an intermediate nonequilibrium correlated metal monoclinic (MCM) state [24–27]. Meanwhile, others have reported an electron correlation driven MIT without the detection of a corresponding structural transition under certain circumstances [28,29].

Resolving the issue of decoupled phase transitions is complicated by material quality issues compounded by the lack of bulk sensitive techniques that can simultaneously measure the electronic and geometric structure. In addition, there are serious limitations of band theory for describing VO_2 phases. Structural inhomogeneity in VO_2 can arise from a mismatch between the film and substrate structure,

resulting in an assortment of domains with differing orientation and strain. Since the VO_2 transition temperature is dependent on strain [21,30], the $M1$, $M2$, and R phases can all readily coexist within these lower quality, polycrystalline films [31]. Meanwhile, slight differences in composition can also drastically alter the properties of these thin films, which is extremely problematic for surface-sensitive techniques requiring any sort of elevated temperature surface preparation. For example, the abruptness of the MIT is extremely sensitive to stoichiometry [32], and VO_2 will readily reduce during *in vacuo* heating. In addition, even mild annealing when using certain substrates will result in interfacial intermixing that suppresses the MIT [33].

Here, we present temperature-dependent x-ray standing waves (XSW) studies of high quality epitaxial VO_2 films grown on TiO_2, with abrupt interfaces and electronic transitions where the experimental electronic structure and phase diagrams have been described with modeling [21–23,34]. Temperature-dependent XSW provides an opportunity to simultaneously measure the geometric and electronic phase transitions using a single technique. Here the XSW is formed as a result of coherent superposition of an incident and reflected wave under an (hkl) Bragg diffraction condition of the TiO_2 substrate. The wavefront of the XSW is parallel to the (hkl) plane and its period coincides with the (hkl) interplane distance. As the incident photon energy is scanned through the (hkl) reflection, the XSW traverses the VO_2 lattice not only ejecting photoelectrons that encode the electronic structure of the sublattices but also modulating the V and O photoelectron intensity yields depending on the positions of the emitters along the (hkl) direction. The combination of XSW with hard x-ray photoelectron spectroscopy (HAXPES) thus allows us to simultaneously access the geometric and electronic structures across the MIT.

Our XSW study of epitaxially strained $VO_2/TiO_2(001)$, supported by our modeling of the endpoint phase spectral functions, highlights how the electronic transition is intimately linked with a structural transition (i.e., dimerization) between the $M1$ and R phases. Taken together with similar findings for V_2O_3 [14], one can conclude that electron correlations in these "Mott" systems do not supersede their accompanying structural transition in importance, but instead cooperatively transition the material between phases. Our experiments reveal the intrinsic interplay between the lattice and orbital degrees of freedom in this class of materials.

Methods.—High-quality VO_2/TiO_2 films were epitaxially grown on TiO_2 substrates by reactive molecular-beam epitaxy (MBE) [35,36]. These films display an abrupt change of resistance by 3 orders of magnitude characteristic of the first-order transition of bulk VO_2 and high quality epitaxial films. HAXPES, soft x-ray absorption spectroscopy (XAS), and XSW measurements were carried out at beam line I09 at the Diamond Light Source (see Supplemental Material for experimental details [36]). Density functional theory (DFT) calculations were produced within the WIEN2K [42] ecosystem using the mBJ [43] functional approximation after including important structural considerations to reliably represent strained VO_2 [36]. Meanwhile, O K-edge XAS simulations of the insulating ($M1$) and metallic (rutile) VO_2 structure phase were carried out using the Quantum ESPRESSO software package [44] within the determinant formalism, an extended delta-self-consistent-field (ΔSCF) method [45,46] where many-body effects are included by single or multiple electron-hole (e-h) excitations (see Supplemental Material [36] for more details on the extended ΔSCF method). The determinant formalism is implemented in the ShirleyXAS and MBXASPY software [47].

Results and discussion.—The choice of growth orientation is of substantial importance in the study of coupling between a SPT and a MIT due to the sensitivity of electron correlation to strain. Figure 1 compares the expected ratios of the equatorial to apical V-O bond distances of the two rutile sublattices (V_1 and V_2) and the unit cell deformation (bandwidth modulation of the characteristic Mott ratio parameter) for the different R-VO_2/TiO_2 strain orientations. These ratio parameters are an elegant electron correlation gauge for strained thin films [23]. Consistent with these critical descriptors, the (100) and (110) orientations of TiO_2 have been found to result in a strain-induced orbital selective Mott transition (OSMT) in VO_2, giving rise to an intermediate strained-stabilized $M2$ phase between the $M1$ to R end points of the SPT. The emergence of $M2$ is also a characteristic signature of stronger electron correlations compared to bulk VO_2 [21,22]. Furthermore, the addition of a second insulating phase can resolve in coexisting domains of the $M1$, $M2$, and R phase [31,48] complicating the XSW structure analysis, conversely to

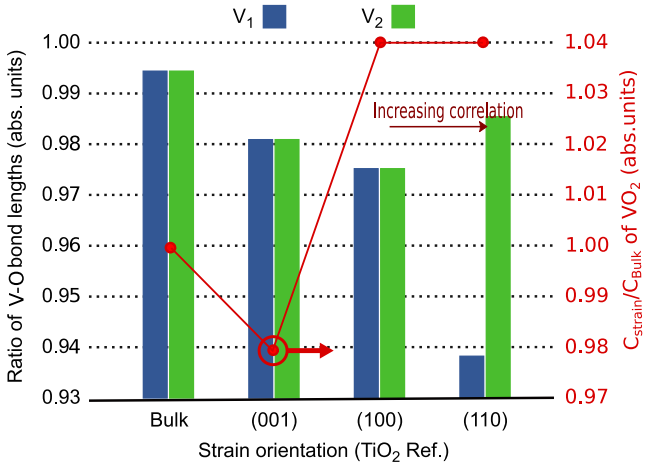

FIG. 1. For (VO_6) octahedra in a VO_2 rutile structure, bars indicate the ratio of equatorial to apical oxygen to vanadium distances of the two distinct octahedra V_1 and V_2 [49] for growth on different TiO_2 orientations. The (001) orientation is the most similar to bulk VO_2 in terms of electron correlation strength [22].

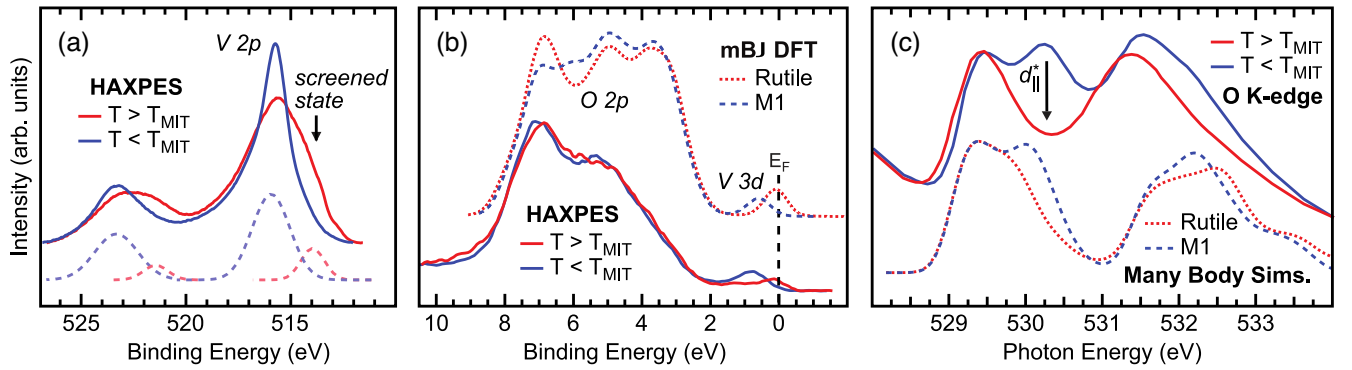

FIG. 2. Temperature-dependent HAXPES ($h\nu \approx 6$ keV) of 10 nm thick $VO_2/TiO_2(001)$ below and above the transition temperature for the (a) V $2p$ core region and (b) valance band region. (c) O K-edge absorption (TEY mode) compared to XAS simulations including many-body effects up to the second order of approximation. The $d^*_{||}$ state associated with dimer formation is denoted.

(001) in which its epitaxially induced c-axis compression in the VO_2 top layer sets the transition away from the coexisting triple point into a bulklike $M1$ to R transition [18]. X-ray spectroscopy studies of VO_2/TiO_2 (001), which is the most structurally similar to bulk VO_2 in Fig. 1, reveal a bulklike $M1$ to R transition with the difference in transition temperature being accounted for by considering biaxial strain in Ginzburg Landau calculations [21,34].

Figure 2 shows the end points of our epitaxial VO_2 agree with the simulations of bulk electronic structure. The metal and insulating states are well distinguished in both the core level and valence band region, providing a direct measurement of the metallicity of the system.

Evidence of the high temperature metallic state is confirmed by HAXPES of the V $2p$ core level [Fig. 2(a)] and the valence band region [Fig. 2(b)]. Metallic VO_2 is demonstrated by an asymmetric broadening to lower binding energies of the V $2p$ core state referred to as screened states, which is a consequence of the positive coulomb potential of the photoelectron hole in the V $2p$ state being screened by electrons at states by the Fermi energy [50,51]. This screening effect is consistent with the metallic screening effect discussed in a previous report on the NbO_2 MIT [52] and provides a direct probe of the states at the Fermi level as shown in the other orientations (see Supplemental Material [36].) The screened state spectral weight is computed through peak fitting with the dashed peaks in Fig. 2(a).

The VO_2 insulating $M1$ phase displays characteristic signatures of splitting between the vanadium dimer bonding $d_{||}$ and antibonding $d^*_{||}$ states, which are observed in the HAXPES valance band [Fig. 2(b)] and O K-edge XAS [Fig. 2(c)], respectively.

Figures 2(b) and 2(c) show the spectroscopic signatures of the endpoint R and $M1$ phases are reproduced by density functional theory of the bulk end point phases of VO_2 using the mBJ approximation and by many body simulations of the O K-edge using second order corrections [36]. The fact that the mBJ functional manages to reproduce the insulating $M1$ phase using structural destabilization (Peierls dimerization) of the metallic R phase strongly suggests that in this strained epitaxial VO_2/TiO_2 (001) system, the MIT is likely cooperative driven by a structure distortion in conjunction with electron correlation [22,23]. To a certain extent, the latter is accounted for by the nature of the orbital-dependent potentials of the mBJ functional [53]. More explicit treatments of the on-site Coulombic interactions beyond hybrid DFT need to be taken into account for a full consideration of correlation effects for the other strain orientations [23].

The inherent coupling of the structural and electronic transition is shown by our temperature-dependent studies summarized in Fig. 3. The temperature-dependent resistivity of the $VO_2/TiO_2(001)$ shown in Fig. 3(a) is consistent with the literature [29,54]. The corresponding temperature-dependent photoemission spectroscopy of the topmost V 3d states is consistent with this abrupt first-order transition in the resistivity. Figure 3(b) shows the abrupt disappearance of a metallic Fermi edge at T_{MIT}, with no evidence of an intermediate phase.

Figure 3(c) shows a schematic representation of the XSW technique for the end point structures, capable of simultaneously measuring both the geometric and electronic transitions. The structural transition is captured by changes in the amplitude (coherent fraction) and phase (coherent position) of the (hkl) Fourier components of the periodic atomic distribution of V or O within the escape depth of the photoelectrons [55,56]. The coherent position can be interpreted as the average position of the emitters relative to the substrate extrapolated (hkl) planes in units of the interplane spacing. The coherent fraction then provides a measure of sharpness of the distribution of the emitters. XSW is thus highly sensitive to the structural changes in VO_2 across the transition temperature. Meanwhile, photoelectrons generated by the x-ray standing wave within the sample can be used to measure the occupied electronic states of chosen atomic species, as shown in Fig. 2(a).

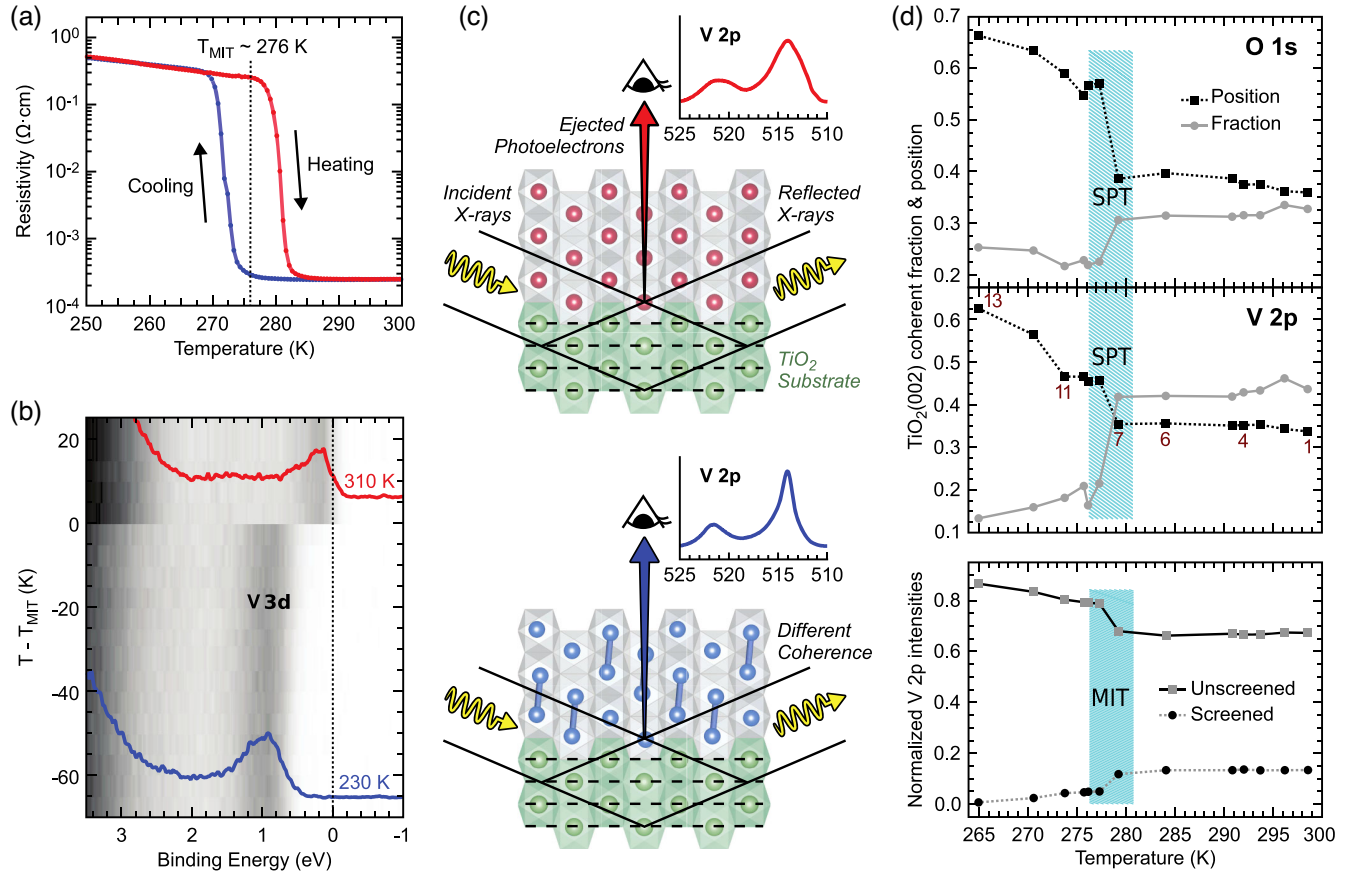

FIG. 3. (a) Temperature-dependent resistivity measurements of a representative 15 nm VO_2/TiO_2 (001) film. The MIT transition is centered around ~276 K. (b) Temperature-dependent HAXPES at the Fermi level of 10 nm VO_2/TiO_2 (001) heated through the MIT temperature. (c) Schematic depiction of the x-ray standing wave experiment. Note that the actual experiment was carried out in a normal incidence geometry. (d) X-ray standing wave results for 10 nm VO_2/TiO_2 (001) through the MIT temperature. Intensities were normalized with the area under the curve before a peak fitting process to acquire the spectral fraction for screened states. The coherent fraction and position were calculated through data fitting (see Supplemental Material [36].)

In our experiment the photon energy was tuned to 4.19 keV to excite the TiO_2 (002) Bragg reflection, forming an x-ray standing wave perpendicular to the sample surface with a periodicity matching the TiO_2 (002) interplane distance. The temperature dependence of the screened and unscreened V $2p$ intensities as well as the (002) coherent fraction and position for V and O deduced from the XSW measurements are plotted in Fig. 3(d). XSW simulations show that, as the system is cooling down across the SPT, the coherent position P_{002} of V in the strained VO_2 film should increase from 0.33 to 0.45 because of an increased interplane distance in the R to $M1$ phase transition amplified by the stacking of 35 VO_2 unit cells in the 10 nm film. These simulations are in excellent agreement with the XSW result [Fig. 3(d), middle], where the observed V P_{002} changes from 0.35 (T_1-T_7) to 0.46 (T_8-T_{11}). A comparable but larger jump is measured for the O P_{002} [Fig. 3(d), top]. In parallel to the SPT occurring in the 2 K window between T_7 and T_8, the electronic transition is observed by the sudden disappearance of the characteristic screened state in the V $2p$ spectrum [Fig. 3(d), bottom] (see Supplemental Material [36] for more details on our XSW simulations and a full interpretation of the XSW results.)

In Fig. 3(d), the screened and unscreened V $2p$ intensities as well as the V and O P_{002}'s exhibit a plateau over the first 5 K below the SPT (T_8—T_{11}), where our XSW analysis confirms that the $M1$ VO_2 remains fully strained to the substrate. However, at further lower temperatures, partial relaxation of the $M1$ VO_2 rises the V and O P_{002} (T_{12} and T_{13}) given by a larger expansion of the normal interplane distance (see Supplemental Material [36]). Figure 3(d) shows that this strain relaxation process occurs in tandem with a gradual evolution of the screened or unscreened V $2p$ intensity, a behavior that has also been observed in thicker VO_2 films regardless of heating and cooling (see Supplemental Material [36]) and that further demonstrates the inherent coupling between the geometric and electronic transitions in VO_2.

Conclusion.—The x-ray standing wave technique elegantly demonstrates how the SPT and MIT of VO_2/TiO_2 (001) are inherently coupled, without any evidence of a

new intermediate phase despite non-negligible electron correlations [23]. We chose the (001) orientation for this study because it possesses a transition most similar to that of bulk VO_2 [20,22,23,34]. Our mBJ DFT calculations, HAXPES, and O K-edge XAS all support bulklike end point phases. Meanwhile, our T-XSW precludes the possibility of decoupled phases, consistent with the Landau-Ginzburg theory predicted phase diagram of VO_2/TiO_2 (001) [21]. It is important to note that due to the high lattice mismatch involved, thicker (and thus partially relaxed) epitaxial VO_2/TiO_2 (001) samples can display strain gradients [30] that smear results, making it difficult to resolve an abrupt SPT or MIT even when using XSW. In addition, we note that for more correlated materials like V_2O_3, the MIT has also been shown in the literature to be coupled with a structural transition [14]. Taken together, these results indicate that even in systems where the MIT is considered to be mainly driven by Mott physics, such as biaxially strained VO_2 [22,23], the contribution of other degrees of freedom should not be discarded ipso facto. As such, structural transitions must be considered as an unavoidable part of the switching mechanism of vanadium-oxide-based "Mott memristors."

We thank David Prendergast for assistance with XAS simulations. This material is based on the work supported by the Air Force Office of Scientific Research under Award No. FA9550-18-1-0024. This research used resources of the Advanced Light Source and the Molecular Foundry which are U.S. DOE Office of Science facilities at Lawrence Berkeley National Laboratory under Contract No. DE-AC02-05CH11231. We acknowledge Diamond Light Source for time on beamline I09 under Proposals SI13812 and SI25355. G. J. P. acknowledges doctoral degree grant support (Grant No. E0565514) from the Comisión Fulbright Ecuador in conjunction with the Ecuadorian national science department Secretaria de Educacion Superior, Ciencia, Tecnologia e Innovacion (Senescyt). K. T. was supported by a NSF-REU (Grant No. NSF DMR-1658990). For the film synthesis we acknowledge support from the National Science Foundation [Platform for the Accelerated Realization, Analysis, and Discovery of Interface Materials (PARADIM)] under Cooperative Agreement No. DMR-1539918. Substrate preparation was performed in part at the Cornell NanoScale Facility, a member of the National Nanotechnology Coordinated Infrastructure (NNCI), which is supported by the National Science Foundation (Grant No. ECCS-1542081).

*lpiper@binghamton.edu

[1] J. del Valle, P. Salev, F. Tesler, N. M. Vargas, Y. Kalcheim, P. Wang, J. Trastoy, M.-H. Lee, G. Kassabian, J. G. Ramírez, M. J. Rozenberg, and I. K. Schuller, Nature (London) **569**, 388 (2019).
[2] S. Kumar, M. D. Pickett, J. P. Strachan, G. Gibson, Y. Nishi, and R. S. Williams, Adv. Mater. **25**, 6128 (2013).
[3] J. Zhou, Y. Gao, Z. Zhang, H. Luo, C. Cao, Z. Chen, L. Dai, and X. Liu, Sci. Rep. **3**, 1 (2013).
[4] M. A. Kats, R. Blanchard, S. Zhang, P. Genevet, C. Ko, S. Ramanathan, and F. Capasso, Phys. Rev. X **3**, 041004 (2013).
[5] K. B. Ashurov, B. M. Abdurakhmanov, S. C. Iskandarov, T. K. Turdaliev, A. M. Salimboev, M. M. Adilov, and I. J. Abdusaidov, Applied Solar Energy **55**, 119 (2019).
[6] C. Zhang, G. Zhou, J. Wu, Y. Tang, Q. Wen, S. Li, J. Han, B. Jin, J. Chen, and P. Wu, Phys. Rev. Applied **11**, 054016 (2019).
[7] M. Seo, J. Kyoung, H. Park, S. Koo, H.-s. Kim, H. Bernien, B. J. Kim, J. H. Choe, Y. H. Ahn, H.-T. Kim, N. Park, Q.-H. Park, K. Ahn, and D.-S. Kim, Nano Lett. **10**, 2064 (2010).
[8] A. Cavalleri, C. Tóth, C. W. Siders, J. A. Squier, F. Ráksi, P. Forget, and J. C. Kieffer, Phys. Rev. Lett. **87**, 237401 (2001).
[9] Y. Zhou and S. Ramanathan, Proc. IEEE **103**, 1289 (2015).
[10] M. D. Pickett and R. S. Williams, Nanotechnology **23**, 215202 (2012).
[11] M. Imada, A. Fujimori, and Y. Tokura, Rev. Mod. Phys. **70**, 1039 (1998).
[12] N. F. Mott, Proc. Phys. Soc. London Sect. A **62**, 416 (1949).
[13] W. H. Brito, M. C. O. Aguiar, K. Haule, and G. Kotliar, Phys. Rev. Lett. **117**, 056402 (2016).
[14] Y. Kalcheim, N. Butakov, N. M. Vargas, M.-H. Lee, J. del Valle, J. Trastoy, P. Salev, J. Schuller, and I. K. Schuller, Phys. Rev. Lett. **122**, 057601 (2019).
[15] S. A. Corr, D. P. Shoemaker, B. C. Melot, and R. Seshadri, Phys. Rev. Lett. **105**, 056404 (2010).
[16] T. M. Rice, H. Launois, and J. P. Pouget, Phys. Rev. Lett. **73**, 3042 (1994).
[17] R. M. Wentzcovitch, W. W. Schulz, and P. B. Allen, Phys. Rev. Lett. **72**, 3389 (1994).
[18] J. H. Park, J. M. Coy, T. S. Kasirga, C. Huang, Z. Fei, S. Hunter, and D. H. Cobden, Nature (London) **500**, 431 (2013).
[19] M. W. Haverkort, Z. Hu, A. Tanaka, W. Reichelt, S. V. Streltsov, M. A. Korotin, V. I. Anisimov, H. H. Hsieh, H.-J. Lin, C. T. Chen, D. I. Khomskii, and L. H. Tjeng, Phys. Rev. Lett. **95**, 196404 (2005).
[20] T. C. Koethe, Z. Hu, M. W. Haverkort, C. Schüßler-Langeheine, F. Venturini, N. B. Brookes, O. Tjernberg, W. Reichelt, H. H. Hsieh, H.-J. Lin, C. T. Chen, and L. H. Tjeng, Phys. Rev. Lett. **97**, 116402 (2006).
[21] N. F. Quackenbush *et al.*, Phys. Rev. B **94**, 085105 (2016).
[22] S. Mukherjee, N. F. Quackenbush, H. Paik, C. Schlueter, T.-L. Lee, D. G. Schlom, L. F. J. Piper, and W.-C. Lee, Phys. Rev. B **93**, 241110(R) (2016).
[23] W.-C. Lee, M. J. Wahila, S. Mukherjee, C. N. Singh, T. Eustance, A. Regoutz, H. Paik, J. E. Boschker, F. Rodolakis, T.-L. Lee, D. G. Schlom, and L. F. J. Piper, J. Appl. Phys. **125**, 082539 (2019).
[24] H.-T. Kim, Y. W. Lee, B.-J. Kim, B.-G. Chae, S. J. Yun, K.-Y. Kang, K.-J. Han, K.-J. Yee, and Y.-S. Lim, Phys. Rev. Lett. **97**, 266401 (2006).
[25] J. Laverock, S. Kittiwatanakul, A. A. Zakharov, Y. R. Niu, B. Chen, S. A. Wolf, J. W. Lu, and K. E. Smith, Phys. Rev. Lett. **113**, 216402 (2014).

[26] B.-J. Kim, Y. W. Lee, S. Choi, J.-W. Lim, S. J. Yun, H.-T. Kim, T.-J. Shin, and H.-S. Yun, Phys. Rev. B **77**, 235401 (2008).
[27] F. Grandi, A. Amaricci, and M. Fabrizio, Phys. Rev. Research **2**, 013298 (2020).
[28] M. Yang, Y. Yang, Bin Hong, L. Wang, K. Hu, Y. Dong, H. Xu, H. Huang, J. Zhao, H. Chen, L. Song, H. Ju, J. Zhu, J. Bao, X. Li, Y. Gu, T. Yang, X. Gao, Z. Luo, and C. Gao, Sci. Rep. **6**, 23119 (2016).
[29] S. Kittiwatanakul, S. A. Wolf, and J. Lu, Appl. Phys. Lett. **105**, 073112 (2014).
[30] L. L. Fan, S. Chen, Z. L. Luo, Q. H. Liu, Y. F. Wu, L. Song, D. X. Ji, P. Wang, W. S. Chu, C. Gao, C. W. Zou, and Z. Y. Wu, Nano Lett. **14**, 4036 (2014).
[31] M. M. Qazilbash, M. Brehm, B.-G. Chae, P.-C. Ho, G. O. Andreev, B.-J. Kim, S. J. Yun, A. V. Balatsky, M. B. Maple, F. Keilmann, H.-T. Kim, and D. N. Basov, Science **318**, 1750 (2007).
[32] D. Lee *et al.*, Science **362**, 1037 (2018).
[33] N. F. Quackenbush, H. Paik, M. E. Holtz, M. J. Wahila, J. A. Moyer, S. Barthel, T. O. Wehling, D. A. Arena, J. C. Woicik, D. A. Muller, D. G. Schlom, and L. F. J. Piper, Phys. Rev. B **96**, 081103(R) (2017).
[34] N. F. Quackenbush, J. W. Tashman, J. A. Mundy, S. Sallis, H. Paik, R. Misra, J. A. Moyer, J.-H. Guo, D. A. Fischer, J. C. Woicik, D. A. Muller, D. G. Schlom, and L. F. J. Piper, Nano Lett. **13**, 4857 (2013).
[35] H. Paik, J. A. Moyer, T. Spila, J. W. Tashman, J. A. Mundy, E. Freeman, N. Shukla, J. M. Lapano, R. Engel-Herbert, W. Zander, J. Schubert, D. A. Muller, S. Datta, P. Schiffer, and D. G. Schlom, Appl. Phys. Lett. **107**, 163101 (2015).
[36] See Supplemental Material at http://link.aps.org/supplemental/10.1103/PhysRevLett.124.196402 for experimental details of HAXPES, XAS, XSW, and film growth; for the theoretical structural considerations for strained materials and simulation details on HAXPES, soft XAS, and XSW; for arguments supporting a lower metallic screening on V $2p$ spectral weight in different growth orientations; for a detailed guidance on how the coherent fraction and position are calculated; and for details regarding the strain gradient effects of coherent fraction measurements in thicker films. It includes Refs. [37–41].
[37] J. B. Goodenough, Prog. Solid State Chem. **5**, 145 (1971).
[38] A. Zylbersztejn and N. F. Mott, Phys. Rev. B **11**, 4383 (1975).
[39] Z. Zhu and U. Schwingenschlögl, Phys. Rev. B **86**, 075149 (2012).
[40] P. Giannozzi *et al.*, J. Phys. Condens. Matter **21**, 395502 (2009).
[41] J. Zegenhagen, Jpn. J. Appl. Phys. **58**, 110502 (2019).
[42] P. Blaha, K. Schwarz, G. K. H. Madsen, D. Kvasnicka, and J. Luitz, *WIEN2K, An Augmented Plane Wave +Local Orbitals Program for Calculating Crystal Properties* (Karlheinz Schwarz, Techn. Universität Wien, Austria, 2001).
[43] D. Koller, F. Tran, and P. Blaha, Phys. Rev. B **85**, 155109 (2012).
[44] P. Giannozzi *et al.*, J. Phys. Condens. Matter **29**, 465901 (2017).
[45] Y. Liang, J. Vinson, S. Pemmaraju, W. S. Drisdell, E. L. Shirley, and D. Prendergast, Phys. Rev. Lett. **118**, 096402 (2017).
[46] Y. Liang and D. Prendergast, Phys. Rev. B **97**, 205127 (2018).
[47] The referred softwares are available at https://github.com/yufengliang/mbxaspy.
[48] J. I. Sohn, H. J. Joo, D. Ahn, H. H. Lee, A. E. Porter, K. Kim, D. J. Kang, and M. E. Welland, Nano Lett. **9**, 3392 (2009).
[49] V. Eyert, Ann. Phys. (Amsterdam) **11**, 650 (2002).
[50] M. Taguchi, A. Chainani, N. Kamakura, K. Horiba, Y. Takata, M. Yabashi, K. Tamasaku, Y. Nishino, D. Miwa, T. Ishikawa, S. Shin, E. Ikenaga, T. Yokoya, K. Kobayashi, T. Mochiku, K. Hirata, and K. Motoya, Phys. Rev. B **71**, 155102 (2005).
[51] R. Eguchi, M. Taguchi, M. Matsunami, K. Horiba, K. Yamamoto, Y. Ishida, A. Chainani, Y. Takata, M. Yabashi, D. Miwa, Y. Nishino, K. Tamasaku, T. Ishikawa, Y. Senba, H. Ohashi, Y. Muraoka, Z. Hiroi, and S. Shin, Phys. Rev. B **78**, 075115 (2008).
[52] M. J. Wahila, G. Paez, C. N. Singh, A. Regoutz, S. Sallis, M. J. Zuba, J. Rana, M. B. Tellekamp, J. E. Boschker, T. Markurt, J. E. N. Swallow, L. A. H. Jones, T. D. Veal, W. Yang, T.-L. Lee, F. Rodolakis, J. T. Sadowski, D. Prendergast, W.-C. Lee, W. A. Doolittle, and L. F. J. Piper, Phys. Rev. Mater. **3**, 074602 (2019).
[53] Z. Zhu and U. Schwingenschlögl, Phys. Rev. B **86**, 075149 (2012).
[54] T. Yao, X. Zhang, Z. Sun, S. Liu, Y. Huang, Y. Xie, C. Wu, X. Yuan, W. Zhang, Z. Wu, G. Pan, F. Hu, L. Wu, Q. Liu, and S. Wei, Phys. Rev. Lett. **105**, 2 (2010).
[55] J. Zegenhagen, Surf. Sci. Rep. **18**, 202 (1993).
[56] D. Woodruff, Prog. Surf. Sci. **57**, 1 (1998).

Simultaneous Structural and Electronic Transitions in Epitaxial VO_2/TiO_2 (001)

Galo J. Paez,[1] Christopher N. Singh,[1] Matthew J. Wahila,[2] Keith E. Tirpak,[1] Nicholas F. Quackenbush,[1] Shawn Sallis,[2] Hanjong Paik,[3,4] Yufeng Liang,[5] Darrell G. Schlom,[3,6] Tien-Lin Lee,[7] Christoph Schlueter,[7] Wei-Cheng Lee,[1] and Louis F. J. Piper[1,2,*]

[1]*Department of Physics, Binghamton University, State University of New York, Binghamton, NY 13850, USA*
[2]*Materials Science and Engineering, Binghamton University, State University of New York, Binghamton, NY 13850, USA*
[3]*Department of Materials Science and Engineering, Cornell University, Ithaca, New York 14853-1501, USA*
[4]*Platform for the Accelerated Realization, Analysis, and Discovery of Interface Materials (PARADIM), Cornell University, Ithaca, New York 14853, USA*
[5]*The Molecular Foundry, Lawrence Berkeley National Laboratory, Berkeley, California 94720, USA*
[6]*Kavli Institute at Cornell for Nanoscale Science, Ithaca, New York 14853, USA*
[7]*Diamond Light Source Ltd., Harwell Science and Innovation Campus, Didcot OX11 0DE, UK*

I. EXPERIMENTAL DETAILS

A. Sample growth

A set of epitaxial VO_2 thin films were grown on rutile (001) TiO_2 single crystal substrates (CrysTec GmbH, Germany) by reactive molecular-beam epitaxy (MBE) in aVeeco GEN10. Substrates were prepared by etching and annealing to have clean and well-defined step and terrace micro-structured surfaces. Vanadium and distilled ozone were codeposited onto the substrate held at 250 °C under a distilled ozone background pressure of 1.0×10^{-6} Torr. Following deposition of the desired 10, 15, and 30 nm film thickness, the temperature of the sample was rapidly ramped to 350 °C, then immediately cooled to below 100 °C under the same background pressure of distilled ozone to achieve an improved film smoothness and a more abrupt MIT.

B. X-ray spectroscopy

Hard X-ray photoelectron spectroscopy (HAXPES) measurements of core regions were performed in Diamond beamline I09 using photon energy of 5.934 keV and a pass energy of 200 eV, with a corresponding resolution better than 200 meV. The binding energy axes were referenced to both the Au $4f_{7/2}$ and Fermi edge of a Au foil in electrical contact with the film. X-ray standing wave data was also collected at Diamond beamline I09 using photon energy of 4.19 keV at the (002) Bragg condition of substrate TiO_2 of VO_2/TiO_2 films. Coherent fraction and position represents the Fourier amplitude and phase components of a periodic atomic distribution given by the atoms in the spatial periodic planes. The total electron yield (TEY) mode of Soft x-ray absorption of VO_2/TiO_2 was also at Diamond beamline I09. To account for beam irregularities, the absorption signal was divided by the signal from a reference Au-coated mesh (I_0) in the incident photon beam.

* lpiper@binghamton.edu

II. COMPUTATIONAL METHOD DETAILS

A. Theoretical considerations for film straining effect simulation

As mentioned, a proper study of the VO_2 metal-insulator transition requires two things: a sample that accurately represents the bulk, and a theoretical treatment of the as-grown sample. Epitaxial films offer the highest quality material, and the XSW technique captures electronic and ionic information simultaneously. Together these address the experimental requirement, but the theory is left wanting.

The theoretical treatment however is not straightforward for two reasons. The first challenge is the epitaxially-matched film will be under great strain. So care must be taken to disentangle observations in strained samples from manifestations of bulk properties. For a consistent description, we must be able to adiabatically connect the three growth orientations. Using TiO_2 as a substrate, we determine space group 6 (Pm) as the lowest common Bravais lattice for the (001), (100), and (110) films, ensuring no artificial symmetry is retained or broken in the analysis.

The canonical approach to determining the new lattice parameters induced by epitaxial strain is to assume volume conservation. The lattice parameters for the (001) and (100) growth orientations can be calculated straightforwardly in the original rutile atomic basis because it is commensurate with the rutile TiO_2 symmetry. In order to simulate the (110) growth condition however, a linear map is applied to the VO_2 basis defined by

$$\hat{\mathcal{M}} = \begin{pmatrix} 1 & 1 & 0 \\ -1 & 1 & 0 \\ 0 & 0 & 1 \end{pmatrix}. \tag{1}$$

This defines the growth direction along the crystallographic b-axis. To determine the new lattice vectors, the same map $\mathcal{M}$ is applied to the TiO_2 lattice vectors, the in plane vectors are matched, and the out of plane vector is determined assuming volume conservation. Then the inverse map $\mathcal{M}^{-1}$ is applied. This procedure keeps the atomic basis and Bravais lattice the same, but changes the lattice vectors and the angles.

B. HAXPES Simulations

The second challenge is that a single-particle description of the vanadium $3d$-manifold is notoriously inadequate. A strained crystal structure complicates the molecular orbital picture proposed early on by Goodenough because octohedral distortions break cubic ligancy. The result is five, non-degenerate, d orbitals and an additional non-equivalent vanadium position [1, 2]. Beyond single particle descriptions are rarely tractable for ten orbital systems. The many outstanding first principles studies of VO_2 have shown that only one approximation to the exchange correlation energy, mBJ [3], captures seamlessly all the features of metal-insulator transition including the gap, magnetic order, energy hierarchy, et cetera [4]. For this reason, we take the mBJ functional as the best approximation for a first principles analysis of VO_2. The electronic structure simulations were performed within the WIEN2k [5] ecosystem. A 20,000 kpoint Brillouin zone sampling was used with an RKmax of 7.2. The RMT's were fixed to 1.82 and 1.65 a.u for vanadium and oxygen respectively, and the GMAX was set to 14. This is necessary so that the mixed basis sets used in the computation are consistent. Spin orbit coupling is known to be a negligible energy scale, and no magnetic ordering was stabilized [4].

C. Soft XAS Simulations

The simulation of the X-ray absorption spectra was done using the PWscf code in the Quantum ESPRESSO software package [6]. The spectral simulation was done using the excited electron core-hole (XCH) approach in which an electron is removed from the inner shell of a designated excited atom within a supercell to account for excited state core-hole interactions. The core-hole perturbation is not explicitly included and is instead accounted for using a modified oxygen pseudopotential with one electron removed from the 1s orbital for the O K-edge. The excited electron is then added to the occupied electronic structure. Finally, the modified electronic system is relaxed to its ground state using DFT. The many-body XAS spectra were simulated using the determinant formalism implemented in the ShirleyXAS and MBXASPY software codes [7, 8]. We utilized a $2 \times 2 \times 3$ supercell structure for rutile VO_2 calculations and a $2 \times 2 \times 2$ super cell for the M_1 phase calculations. All supercells were chosen such that their dimensions were large enough to avoid effects due to neighboring periodic images and the spectra from all inequivalent oxygen positions were calculated and averaged to produce the final spectra.

D. XSW Simulations

The spatial atomic distribution of V or O in the VO_2 film can be expressed as a Fourier series based on the periodicity of the substrate TiO_2 lattice. The coefficient of the Fourier component corresponding to a TiO_2 (002) reflection in this expansion is

$$G_{hkl} = f_{hkl} \exp(2\pi i P_{hkl}) \tag{2}$$

, where f_{hkl} and P_{hkl} are the so-called coherent fraction and coherent position, respectively, for the (hkl) reflection. Broadly speaking, P_{hkl} measures the center of the distribution along the (hkl) direction in units of the TiO_2 interplane distance $d_{(hkl)}^{TiO_2}$ and f_{hkl} the sharpness of the distribution around P_{hkl}. f_{hkl} is a number between 0 and 1 with f_{hkl}=1 representing a delta-function-like distribution and f_{hkl}=0 a disordered structure (in which case the P_{hkl} is undefined).

For VO_2 in the rutile phase V and O occupy two positions per unit cell along the c axis that are separated by $c^{VO_2-R}/2$. There are thus $2N$ V or O layers in a VO_2 film of N unit cells. The (002) Fourier coefficient of such a film is the weighted sum of the (002) Fourier coefficients of the individual layers

$$G_{002} = f_{002} \exp(2\pi i P_{002}) = \frac{1}{\Sigma w^n} \Sigma_{n=1}^{2N} w^n f_{002}^n \exp(2\pi i P_{002}^n) \tag{3}$$

, where $f_{002}^n \exp(2\pi i P_{002}^n)$ is the (002) Fourier coefficient of the nth atomic layer and $w^n = \exp\left(-(2N-n)c^{VO_2-R}/2\lambda\sin(\theta)\right)$ a weighting factor accounting for the attenuation of photo-electrons emitted from that layer, with $\lambda \approx 55$ Å and $\theta \approx 18$ ° being the inelastic mean free path of 3665 eV electrons (V 2p and O 1s) through VO_2 and the average emission angle with respect to the sample surface. $f_{002}^n = 1$ for all layers if we assume an ideal rutile structure for the VO_2 film and ignore the contribution of thermal vibration. P_{002}^n can be calculated as

$$P_{002}^n = \left(\Delta^{interface} + nc^{VO_2-R}/2\right)/d_{002}^{TiO_2} = \left(2\Delta^{interface} + nc^{VO_2-R}\right)c^{TiO_2} \tag{4}$$

, where $\Delta^{interface}$ is the distance between VO_2 and TiO_2 at the interface in addition to $c^{VO_2-R}/2$.

The table S1 lists the lattice constants of bulk rutile TiO_2 and VO_2, bulk M1 VO_2, and rutile and M1 VO_2 (001) thin films epitaxially grown on TiO_2 (001) [9, 10].

	Rutile TiO_2	Rutile VO_2			M1 VO_2	
	Bulk	Bulk	(001) film on TiO_2 (001)		Bulk	(001) film on TiO_2 (001)
a	4.594	4.5546	4.594	b	4.517	4.594
b	4.594	4.5546	4.594	c*sin 57.4°	4.528	4.594
c	2.958	2.8514	$(c^{VO_2-R} =)$ 2.834	a/2	2.872	$(a^{VO_2-M1}/2 =)$ 2.840

TABLE S1. Lattice parameters of bulk rutile TiO_2 and VO_2, bulk M1 VO_2, and rutile and M1 VO_2 (001) thin films epitaxially grown on TiO_2 (001).

The lateral strain of epitaxial rutile VO_2 (001) thin film on TiO_2 (001) is (4.594 - 4.5546)/4.5546 = 0.87%. This stretch of the a and b axes results in a contraction of the c axis that is (2.834 - 2.8514)/2.8514 = -0.61%. In the M1 phase, it is the a axis of VO_2 (001) that is parallel to the c axis of TiO(001) and is approximately twice as long, and the surface cell of VO_2 that needs to register with the TiO_2 (001) surface lattice has the dimensions of $b * c\sin(57.4°)$. The average lateral strain is thus [(4.594-4.517)/4.517+(4.594-4.528)/4.528]/2 = 1.58%, which is 1.82 times the rutile case. It is hence reasonable to assume a change of -0.61%*1.82 = -1.11% to the a axis of bulk M1 phase, leading to $a^{VO_2-M1}/2$ = 2.872*(1-1.11) = 2.840 Å for the strained M1 VO_2 (no experimental data available). Using Eq. 3 and 4 with the above information we find $f_{002} = 0.303$ and $P_{002} = 0.330$ for both V and O for a 10 nm (N = 34) rutile VO_2 (001) film coherently strained to TiO_2 (001), assuming $\Delta^{interface} = 0$.

To consider the strained VO_2 film in the M1 phase, we replace c^{VO_2-R} with $a^{VO_2-M1}/2$ in the formulas. The 10 nm film is now comprised of 17 M1 unit cells, each containing four V and eight O atoms [9], which amount to eight V and sixteen O positions along the TiO_2 (001) direction (or the a axis of M1 VO_2). We have modified Eq. 3 and 4 to take all these positions into account. We find $f_{002} = .280$ and $P_{002} = 0.459$ for V and $f_{002} = .316$ and $P_{002} = 0.442$ for O. We summarize our calculations in the table S2.

Our calculations show that across the SPT from the rutile to the M1 phase the P_{002} of V is expected to increase from 0.33 to about 0.45, in excellent agreement with what we observed in the XSW measurements (276 K - 281 K in Fig. 3 (d)), where P_{002} of V changes from 0.35 to 0.46 when the sample was cooled from 285 to 275 K. Note that this change,

	Rutile VO_2 (001)/TiO_2 (001)	M1 VO_2 (001)/TiO_2 (001)	
	V and O	V	O
f_{002}	0.303	0.280	0.316
P_{002}	0.330	0.459	0.442

TABLE S2. Calculated coherent fraction and position of the strained rutile and M1 VO_2 (001)/TiO_2 (001).

ΔP_{002}, results mainly from the slight increase of VO_2 interplane distance normal to the surface from $c^{VO_2-R}/2$ to $a^{VO_2-M1}/4$, which is then amplified by the stacking of the unit cells to $\Delta P_{002} \approx 34\left(a^{VO_2-M1} - 2c^{VO_2-R}\right)/c^{TiO_2} = 0.14$.

The presence of epitaxial strain reduces significantly the difference between $c^{VO_2-R}/2$ to $a^{VO_2-M1}/4$ and thus ΔP_{002} across the SPT. Yet If the M1 VO_2 film becomes fully relaxed below the SPT, ΔP_{002} is expected to increase considerably to approximately $34\left(a^{VO_2-M1-bulk} - 2c^{VO_2-R}\right)/c^{TiO_2} = 0.87$ (i.e., P_{002} should be about 0.33 + 0.87 = 1.2 below the SPT in this case).

When we cool down the M1 VO_2 film further below the T^{MIT}, the P_{002} of both V and O rise again (270 K and 274 K in Fig. 3 (d). We attribute this to the relaxation of the film, which leads to a higher P_{002} as discussed above. Such relaxation has also been suggested by our previous PEEM studies, where cracks or dislocations were observed to develop in VO_2 films after temperature cycles across the SPT.

Our XSW analysis hence reveals two distinct temperature regions below the SPT in Fig. 3 (d): within about the first 5 K below the SPT, the M1 VO_2 film remains coherently strained to the TiO_2 substrate, as manifested by the P_{002} plateaus measured for V and O; below this 5 K window the M1 VO_2 film starts to relax and expand in the direction normal to the surface, leading to increasing P_{002} (i.e., the film becomes partially relaxed in this temperature range).

To interpret the temperature dependence of f_{002} in Fig. 3 (d) is far more difficult. For the ideal structures of strained rutile and M1 VO_2, our calculations predict essentially no temperature dependence of V and O f_{002} across the SPT, while Fig. 3 (d) shows a significant reduction in f_{002}, particularly for V, crossing the SPT, suggesting degradation of the crystallinity of the film. Our more extensive XSW and PEEM studies further unveil that such structural degradation is irreversible and its extent increases with the number of temperature cycles. These observations reflect the "self-destructive" nature of the SPT and the strain relaxation process in VO_2 thin films. Note that XSW is highly sensitive to the long-range structural integrity of the VO_2 film as our "X-ray ruler" is generated by the high-quality single-crystal TiO_2 substrate, whereas the electronic transition concerns the local structural changes associated with the V-V dimer formation. The SPT induced structural degradation of VO_2 thin films will be discussed in greater detail in a separate paper.

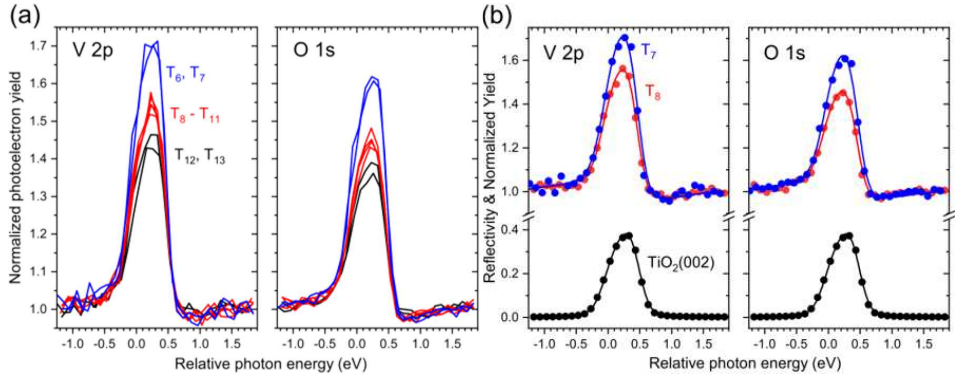

FIG. S1. (a) XSW-modulated V 2p and O 1s photoelectron yields at temperatures before, during, and after T_{MIT}. (b) The best fitted profiles near T_{MIT}.

To demonstrate that XSW has sufficient sensitivity to resolve the small structural change in the SPT of VO_2, we show in Fig. S1 in Panel (a) the XSW-modulated V 2p and O 1s photoelectron yields measured at T_6 to T_{13} and in Panel (b) the best fits to the V 2p and O 1s photoelectron yields and the TiO_2(002) reflectivity (based on dynamical diffraction theory of X-rays) recorded at T_7 and T_8. These figures show that not only the sharp SPT but also the start of the strain relaxation stage is clearly captured by our XSW measurements.

III. EXPERIMENTAL SUPPORT

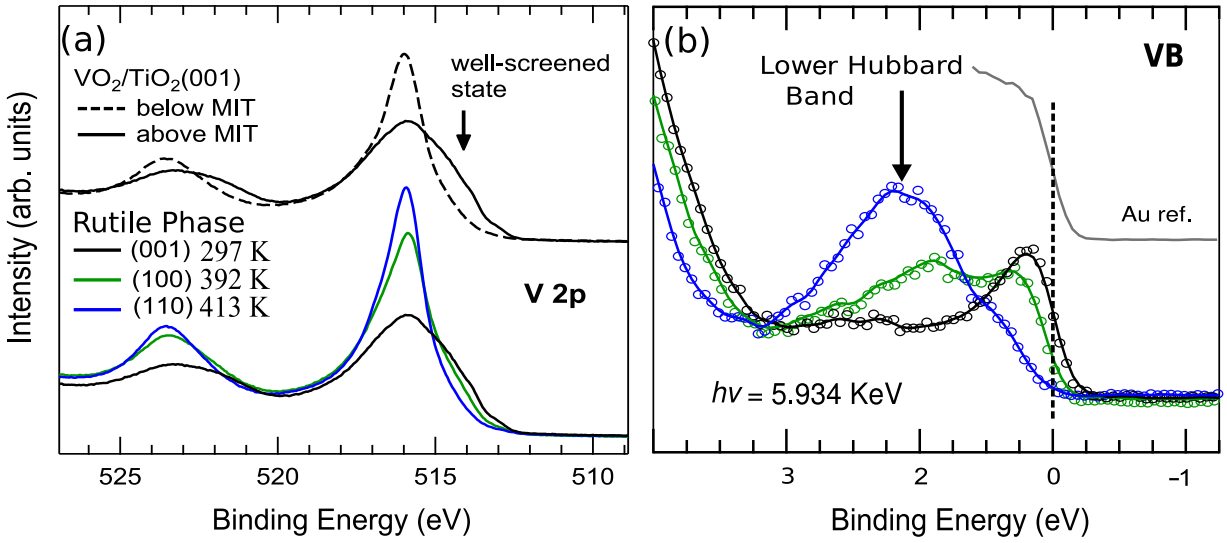

FIG. S2. Temperature-dependent HAXPES ($h\nu \approx 6$ keV) of 10 nm VO_2/TiO_2 at different growth orientation below and above the corresponding transition temperature of each orientation for (a) the V 2p core region and (b) the valence band range. The intensity of the screening effect is proportional to the electronic quasiparticle spectral weight.

Fig. S2 illustrates how the V 2p core level can provide evidence of the states at the Fermi level. Spectral weight screening results when a non-interacting electronic Fermi liquid forms at the Fermi level as a feature of a metallic system state. This Fermi liquid acts as an electronic cloud that collectively response to the potential of a core hole left by the ejected photoelectron during XPS measurements. Consequently, some spectral weight is transferred to spectrum satellites (screened states) at lower V 2p binding energies. However, stronger coulomb correlation in the V 3d states promotes localization of states at ≈ 2 eV as can be seen in Fig. S2 (b) lowering spectral weight at the Fermi level and thus weakening the screening effects. Here, the high temperature phase V 2p data for different orientations show the sensitivity of this core level to states at Fermi level and how stronger correlation effects for the (100) and (110) orientations impact this relationship.

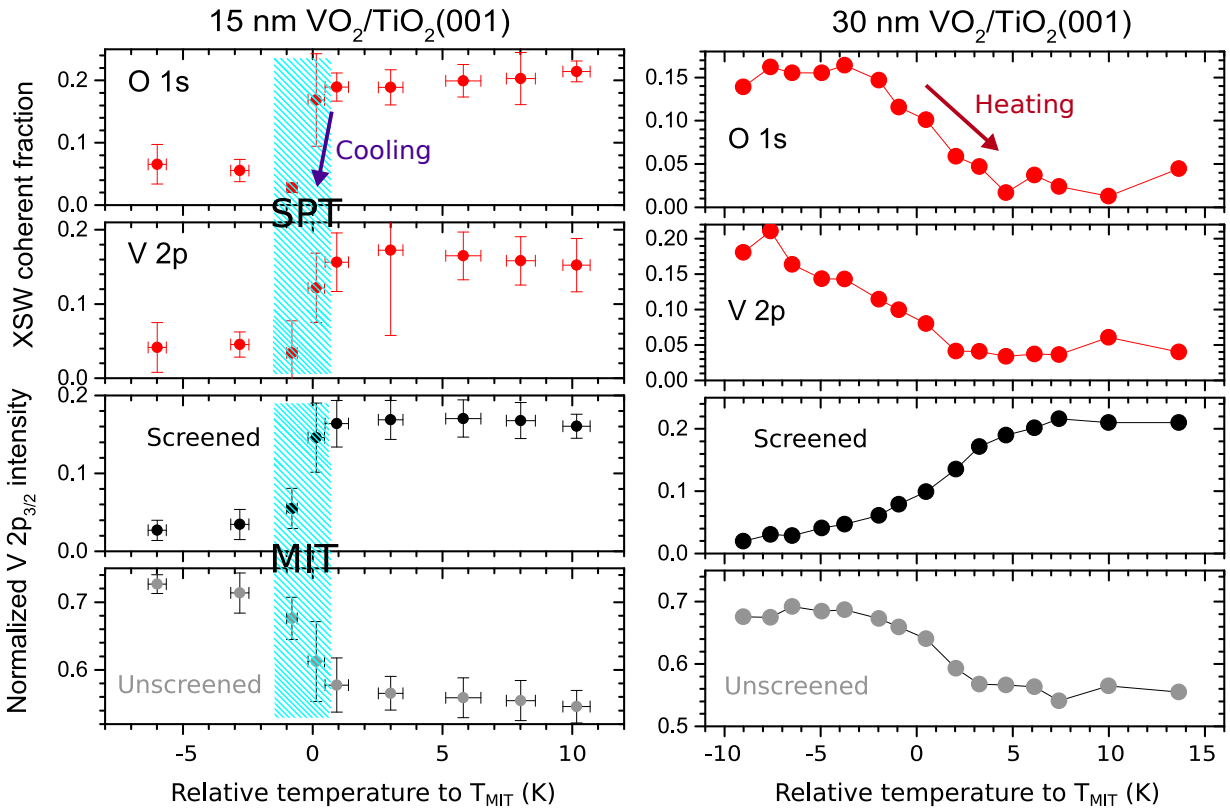

FIG. S3. X-ray standing wave results at 4.19 keV photon energy to develop the rutile TiO_2 (002) Bragg condition for 15 and 30 nm $VO_2/TiO_2(001)$ heated through the MIT temperature.

The XSW coherent fraction and the HAXPES V 2p screened spectral weight fraction both depicted in Fig. S3 shows that the abruptness of the MIT is smeared out as the active layer of VO_2/TiO_2 (001) gets thicker. The 15 nm-thick film measurements were carried out while cooling and the 30 nm-thick film during heating. This effect originates from a strain gradient whose intensity is large near the substrate due to the great biaxial strain at the interface but decays as more VO_2 layers are grown. The strain gradient also creates a gradient of the interlayer spacing between the VO_2 planes parallel to the interface in the epitaxial VO_2/TiO_2 film inducing a natural incoherence between the X-ray standing wave with a fixed spatial periodicity. However, these conditions do not affect the simultaneity of the SPT and MIT since the screened portion of the V2p spectral is still observed as the coherent fraction changes.

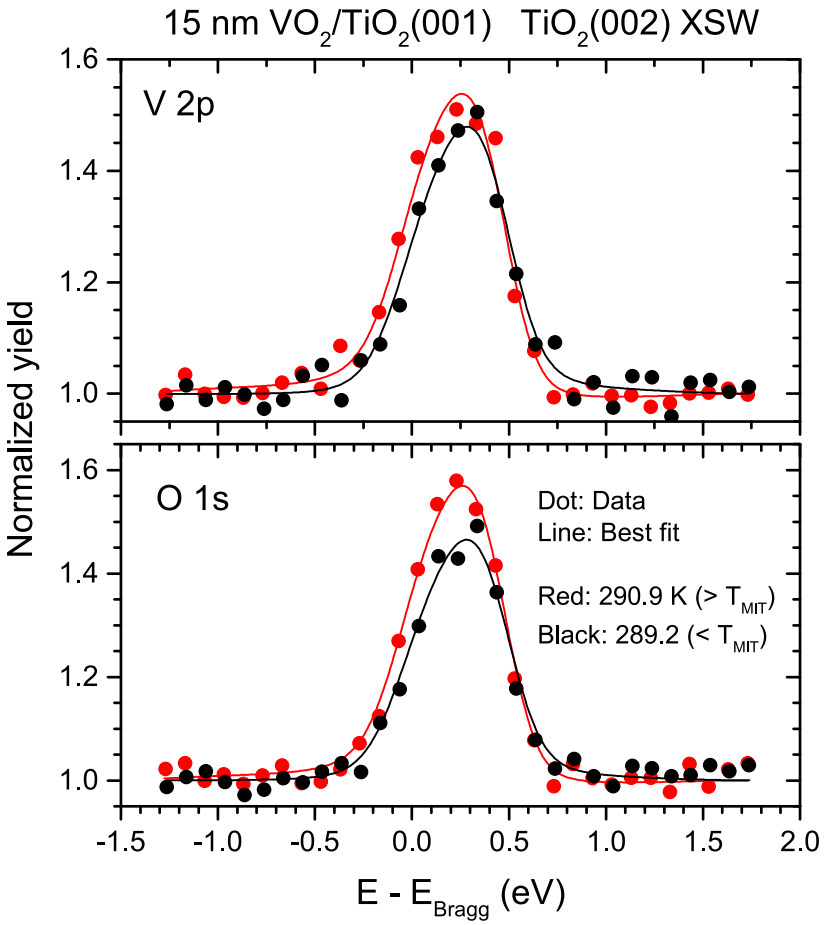

FIG. S4. Photoelectron yield of XSW experiments at room temperature and lower to capture the M1 and R phase photoelectron emission of the V 2p and O 1s state of a 15 nm-thick VO_2/TiO_2 film. A fitting process produces the coherent fraction and position at different temperatures.

The XSW-modulated V 2p and O 1s photoelectron yield profiles and the $TiO_2(002)$ reflectivity curve were recorded while the incident photon energy E_γ was scanned through the $TiO_2(002)$ reflection around 4.19 keV. The photoelectron yield profile can be described by $\left(Y_A(\theta, E_\gamma) = Y_{A,0}\left\{1 + R(\theta, E_\gamma) + 2\sqrt{R(\theta, E_\gamma)}F_A \cos\left[\nu(\theta, E_\gamma) - 2\pi P_A\right]\right\}\right)$ where F_A and P_A are the coherent fraction and position [11, 12]. R and ν are the reflectivity of the $TiO_2(002)$ reflection and the phase of the standing wave, respectively, to be calculated from dynamical theory of X-rays. $\theta \approx 87$ degrees is the incident angle of the X-rays. The best fit of this equation to the photoelectron yield profile determines F_A and P_A. For more details on the analysis of XSW data please see Ref. [13]. The XSW-excited photoelectron profiles were measured at a series of sample temperatures across the MIT of VO_2. At each step the sample temperature was determined by the c lattice constant of the TiO_2 substrate (deduced from the Bragg energy of the $TiO_2(002)$ reflection) and the thermal expansion coefficient of TiO_2 using room temperature as a reference point.

[1] J. B. Goodenough, Progress in solid state chemistry **5**, 145 (1971).
[2] A. Zylbersztejn and N. F. Mott, Phys. Rev. B **11**, 4383 (1975).
[3] D. Koller, F. Tran, and P. Blaha, Phys. Rev. B **85**, 155109 (2012).
[4] Z. Zhu and U. Schwingenschlögl, Phys. Rev. B **86**, 075149 (2012).
[5] P. Blaha, K. Schwarz, G. K. H. Madsen, D. Kvasnicka, and J. Luitz, *WIEN2K, An Augmented Plane Wave + Local Orbitals Program for Calculating Crystal Properties* (Karlheinz Schwarz, Techn. Universität Wien, Austria, 2001).
[6] P. Giannozzi, S. Baroni, N. Bonini, M. Calandra, R. Car, C. Cavazzoni, D. Ceresoli, G. L. Chiarotti, M. Cococcioni, I. Dabo, A. D. Corso, S. de Gironcoli, S. Fabris, G. Fratesi, R. Gebauer, U. Gerstmann, C. Gougoussis, A. Kokalj, M. Lazzeri, L. Martin-Samos, N. Marzari, F. Mauri, R. Mazzarello, S. Paolini, A. Pasquarello, L. Paulatto, C. Sbraccia, S. Scandolo, G. Sclauzero, A. P. Seitsonen, A. Smogunov, P. Umari, and R. M. Wentzcovitch, Journal of Physics: Condensed Matter

21, 395502 (2009).
[7] Y. Liang, J. Vinson, S. Pemmaraju, W. S. Drisdell, E. L. Shirley, and D. Prendergast, Phys. Rev. Lett. **118**, 096402 (2017).
[8] Y. Liang and D. Prendergast, Phys. Rev. B **97**, 205127 (2018).
[9] V. Eyert, Annalen der Physik **11**, 650 (2002).
[10] H. Paik, J. A. Moyer, T. Spila, J. W. Tashman, J. A. Mundy, E. Freeman, N. Shukla, J. M. Lapano, R. Engel-Herbert, W. Zander, J. Schubert, D. A. Muller, S. Datta, P. Schiffer, and D. G. Schlom, Applied Physics Letters **107**, 163101 (2015).
[11] J. Zegenhagen, Surface Science Reports **18**, 202 (1993).
[12] D. Woodruff, Progress in Surface Science **57**, 1 (1998).
[13] J. Zegenhagen, Japanese Journal of Applied Physics **58**, 110502 (2019).